



HAL
open science

Orientation measurements of clay minerals by polarized attenuated total reflection infrared spectroscopy

Brian Gregoire, Baptiste Dazas, Fabien Hubert, Emmanuel Tertre, Eric Ferrage, Laurent Grasset, Sabine Petit

► To cite this version:

Brian Gregoire, Baptiste Dazas, Fabien Hubert, Emmanuel Tertre, Eric Ferrage, et al.. Orientation measurements of clay minerals by polarized attenuated total reflection infrared spectroscopy. *Journal of Colloid and Interface Science*, 2020, 567, pp.274-284. 10.1016/j.jcis.2020.02.021 . hal-03000849

HAL Id: hal-03000849

<https://hal.science/hal-03000849>

Submitted on 24 Nov 2020

HAL is a multi-disciplinary open access archive for the deposit and dissemination of scientific research documents, whether they are published or not. The documents may come from teaching and research institutions in France or abroad, or from public or private research centers.

L'archive ouverte pluridisciplinaire **HAL**, est destinée au dépôt et à la diffusion de documents scientifiques de niveau recherche, publiés ou non, émanant des établissements d'enseignement et de recherche français ou étrangers, des laboratoires publics ou privés.

14 **Abstract**

15 The orientation and organization of molecular guests within the interlayer of clay minerals
16 control the reactivity and performance of tailored organo-clay materials. Such a detailed
17 investigation of hybrid structure on the molecular scale is usually provided by computational
18 methods with limited experimental validation. In this study, polarized attenuated total reflection
19 infrared spectroscopy was used to extract quantitative orientation measurements of
20 montmorillonite particles. The validity of the evanescent electric field amplitude calculations
21 necessary to derive the order parameter was critically evaluated to propose a methodology for
22 determining the orientation of the normal to the clay layer relative to a reference axis, enabling
23 comparison with the results obtained from X-ray scattering experiments and molecular dynamic
24 simulations. Subsequently, the orientation of the interlayer water dipole and surface hydroxyls
25 with respect to the normal of the clay layer was experimentally determined, showing good
26 agreement with molecular simulations. This methodology may provide quantitative insights
27 into the molecular-level description of interfacial processes between organic molecules and clay
28 minerals.

29 **Keywords**

30 Attenuated total reflection spectroscopy; clay minerals; orientation; linear dichroism; thin layer

31 **I. Introduction**

32 The increasing development of methods enabling fine tuning of the nanostructure of materials
33 at the molecular level has strongly contributed to the boost in nanotechnology. Beyond the
34 realm of graphene and its promising commercial potential, other 2D natural-based materials
35 have attracted considerable attention from the scientific community [1]. Owing to their
36 naturally occurring nanoscale structures and associated large surface areas, clay minerals are
37 subjected to increasing interest for numerous applications. For instance, the interactions of clay
38 minerals with colloidal particles or molecular species result in interesting bulk-scale physical
39 and chemical properties. Clay-based nanotechnology has thus led to promising innovation in
40 nanoscience-related fields, such as materials science, electronics, food, and healthcare,
41 contributing to the improvement of human quality of life [2-6]. Their abundance in nature,
42 convenient preparation and biocompatibility are in part responsible for the large quantity of
43 studies devoted to applications of clay minerals.

44 Sodium montmorillonite is certainly one of the most often used clay minerals owing to its low
45 layer charge density, which is responsible for its swelling behavior and exfoliation properties.
46 This material consists of a 2:1 layer composed of two tetrahedral sheets and one octahedral
47 sheet. Isomorphous substitution of aluminum by magnesium in the octahedral sheet produces a
48 negative charge that is counterbalanced by hydrated Na^+ cations located in the interlayer space
49 [7]. The interlayer cations can be further exchanged by a variety of molecules or polymers,
50 conferring the ability to finely tune the functionality of the composite [8-11]. The low charge
51 density of the clay surface and its flat structure at the nanoscale level prevent aggregation of

52 intercalated compounds and further enable molecular control of the molecule-molecule distance
53 and orientation through a size matching effect [12]. This method opens the way for advanced
54 reactivity, such as enantioselectivity and photonic properties. The performance of such
55 materials is strongly dependent on the orientation of the guest molecules, which is sometimes
56 difficult to assess. The molecular orientation is most often derived from the basal spacing
57 obtained from X-ray diffraction (XRD) measurements in comparison with the size and shape
58 of the guest molecules. In some cases, the interlayer domain is highly disordered, preventing
59 local information from being directly obtained through XRD analyses [13]. Further
60 complications arise when more than one single layer is examined when the orientation function
61 of the clay particles has to be equally determined [14, 15]. The preferred orientation of clay
62 particles is of crucial importance, as it controls the geometric properties of the whole porous
63 medium [16] and can vary from almost isotropic to perfectly oriented. The orientational
64 distribution function of clay particles can be experimentally obtained through X-ray diffraction
65 or X-ray microtomography measurements, but these techniques are insensitive to intercalated
66 organic molecules. As a consequence, the interfacial interaction between organics and clay
67 minerals remains inaccessible by these techniques. Vibrational spectroscopies are some of the
68 few molecular-level probes that are inherently orientation sensitive and provide an alternative
69 method for probing the organization of both clay particles and organic molecules in the same
70 preparation [17]. Moreover, Fourier transform infrared (FTIR) spectroscopy allows the study
71 of dynamic processes on a 10^{-14} – 10^{-12} s time scale, which is attainable for molecular dynamic
72 simulations. By explicitly taking into account the particle orientation, the experimental
73 determination of molecular orientation with respect to a clay mineral surface, achievable by

74 FTIR, spectroscopy opens a new way to validate or constrain MD simulations at the molecular
75 level.

76 The absorption of infrared light depends on the mutual orientation of the transition moment and
77 the electric field components. The polarization of infrared light enables the selection of the
78 orientation of the electric field and therefore offers additional control to measure the orientation
79 of molecules and/or clay particles. The transition moments associated with minerals and
80 organics are often well separated in frequency so that independent orientation measurements
81 can be carried out on the same sample. While the literature is rich in studies on molecular
82 orientation determination, little focus has been placed on clay mineral orientation by FTIR
83 spectroscopy. In a recent paper, the general methodology to extract the anisotropic optical
84 constants of Na-montmorillonite by attenuated total reflectance infrared spectroscopy (ATR-
85 FTIR) was presented, and a strong out-of-plane transition moment associated with the Si-O
86 stretching vibration was evidenced [18]. Therefore, such a Si-O stretching vibration band
87 appears to be an adequate descriptor for the determination of the orientation of clay particles.
88 In the few studies devoted to this objective, the authors systematically used thin-film
89 approximation equations for the calculation of the electric field amplitude to derive the order
90 parameter measuring the anisotropy of the clay deposit [19, 20]. To further assess the validity
91 of this approach, the matrix formalism for calculating the electric field amplitude proposed by
92 Hansen, considering the number of layers, the complex refractive index and the deposit
93 thickness, was used and compared with the approximate equations [21, 22].

94 This paper aims to investigate the ability to probe clay orientation by polarized ATR-FTIR
95 spectroscopy. To enable comparison with the results obtained by MD simulations or other
96 experimental techniques, a methodology for determining the orientation of the normal to the
97 clay with respect to a reference axis is proposed. To illustrate the ability to probe the interfacial
98 phenomenon, the orientation of structural hydroxyls and water dipole moments of Na-
99 montmorillonite is experimentally determined and successfully compared to the MD results.

100 **II. Materials and Methods**

101 **II.1. Sample preparation**

102 SWy-3 montmorillonite clay was obtained from the Source Clays Repository of The Clay
103 Minerals Society. Clay with a size of $<1\ \mu\text{m}$ was collected by centrifugation and Na-saturated
104 using three saturation cycles in a 1 M NaCl solution. Excess salt was removed by dialysis until
105 the Cl^- anion was no longer detected by the AgNO_3 test.

106 **II.2. Polarized ATR-FTIR spectroscopy**

107 The ATR-FTIR spectra were recorded on a Nicolet IS50 equipped with a KBr beam splitter and
108 a DLaTGS detector. Polarized radiation was achieved by a ZnSe wire grid polarizer set before
109 the sample compartment. A VeeMax 3 accessory consisting of a thermally controlled horizontal
110 45° single-bounce ATR plate was installed, and the temperature was set at a constant value of
111 $25\ ^\circ\text{C}$ for all experiments. A diluted clay suspension was pipetted and deposited on the Ge IRE

112 (20 mm diameter), and the film was allowed to dry under ambient conditions. Polarized
113 reflectance spectra were acquired at a resolution of 4 cm^{-1} , and 100 scans were coadded.

114 For vibrational bands that are not well resolved, such as the Si-O stretching vibration at 1085
115 cm^{-1} , band fittings of the region $600\text{-}1300\text{ cm}^{-1}$ were applied with a combination of Lorentzian
116 and Gaussian functions, as in Ras *et al.* [19] When band fitting was not necessary, the dichroism
117 ratio was calculated from the maximum intensity.

118 **II.3. Molecular Simulations**

119 The molecular structure of the montmorillonite sample was predicted using grand canonical
120 Monte Carlo (GCMC) and molecular dynamics (MD) simulations at selected hydration states
121 corresponding to the homogeneous one-layer hydrate (1W) and the dehydrated state (0W). The
122 system was composed of three clay sheets (with dimensions of 8-by-5 unit cells in the *ab* plane)
123 and three interlayers. Isomorphic octahedral substitutions of Al^{3+} by Mg^{2+} were randomly
124 distributed in the clay structure to obtain the unit cell formula
125 $^{\text{inter}}[\text{Na}_{0.75}]^{\text{oct}}[\text{Al}_{3.25}\text{Mg}_{0.75}]^{\text{tet}}[\text{Si}_{8.0}]\text{O}_{20}(\text{OH})_4$. The basal spacing was set according to the results
126 of montmorillonite determined by experimental X-ray diffraction modeling [13] of similar
127 samples. Accordingly, the Na-montmorillonite sample shows the least hydration heterogeneity
128 for one layer hydrated at a relative humidity (RH) of 0.4 and under vacuum ($\sim 0\text{RH}$) conditions
129 for the dehydrated state. Consequently, the basal spacing for the present simulations was set, in
130 agreement with the former relative humidity, at 12.46 \AA and 9.75 \AA for the 1W and 0W states,
131 respectively. For both GCMC equilibrium and MD simulations, the following sets of
132 parameters were used. Interatomic interactions were modeled using the SPC/E water model and

133 the CLAYFF model of silicate minerals [23]. The van der Waals “size” parameter of oxygen
134 atoms belonging to the clay layer was increased by 7 % relative to the original CLAYFF model
135 as recommended [24]. Interatomic interactions were calculated in real space up to a distance of
136 15 Å. Beyond this distance, long-range Coulomb interactions were resolved by Ewald
137 summation. Ewald sum calculations were computed with a precision of 10^{-5} .

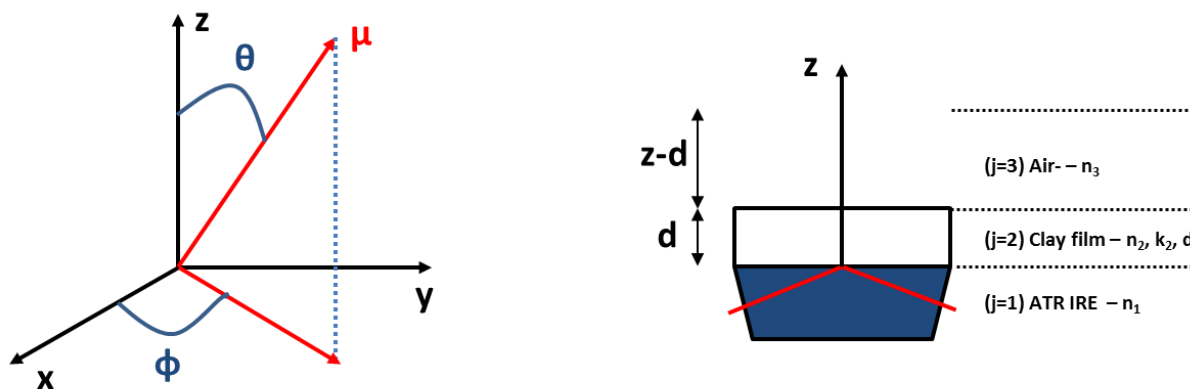
138 The two systems were first equilibrated in the $\mu_{\text{H}_2\text{O}}VT$ ensemble (fixed volume, temperature,
139 and water chemical potential) in the GCMC simulation using a homemade program [24-29].
140 The one-layer hydrates were equilibrated using an RH of 0.4 at 298 K. The target relative
141 humidity was converted to a water chemical potential using the ideal fluid relation $\mu_{\text{H}_2\text{O}} = \mu_{\text{H}_2\text{O}}^0$
142 $+ k_{\text{B}}T \ln(\text{RH})$, where $\mu_{\text{H}_2\text{O}}^0 = k_{\text{B}}T \ln(\Lambda^3 \rho)$, Λ is the de Broglie wavelength of H_2O (0.238376
143 Å), k_{B} is Boltzmann’s constant, T is the absolute temperature, and ρ is the density of water
144 vapor at 298 K (7.7087481×10^{-7} molecules Å⁻³). Each GCMC simulation was carried out for
145 6×10^7 steps. At each step, one of the clay interlayers was selected randomly, and with an equal
146 probability, an attempt was made to remove a H_2O molecule, add a H_2O molecule in a random
147 configuration, or move a randomly chosen Na^+ ion or H_2O molecule. Interlayer water quantities
148 were found to be 4.95. This result is in agreement with previously reported water vapor
149 desorption isotherm experiments on similar samples [30]. For the dehydrated state, no water
150 molecule addition was attempted. Thus, at each step, one of the clay interlayers was selected
151 randomly, and an attempt was made to simply move a randomly chosen Na^+ ion.

152 Thermalized GCMC configurations were used as the starting points for the MD simulations.
153 Molecular dynamics simulations were performed with LAMMPS software [31]. Each

154 simulation cell was first equilibrated in the NVE ensemble (fixed number of atoms, volume and
 155 energy), weakly coupled to a Berendsen thermostat, for a total of 200000 steps at $T = 298$ K.
 156 During these steps, the timestep size for subsequent molecular dynamics simulations was
 157 gradually increased from 0.001 to 0.5 femtoseconds to allow a smooth transition from GCMC
 158 simulations performed with rigid clay layers to MD simulations with flexible layers. Finally,
 159 each system was simulated for 1 nanosecond in the NVE ensemble and weakly coupled to a
 160 Berendsen thermostat with a 0.5 fs timestep at $T = 298$ K.

161 III. Order parameter and mean-squared electric field amplitude calculations

162 a)



163

164 **Figure 1.** a) Definition of the laboratory (xyz) coordinate system used in this paper to define
 165 the transition moments μ from the polar angles θ and ϕ . b) Optical configuration for stratified
 166 layers with two interfaces (three-phase system). The notations are given in the text.

167 Polarized ATR-FTIR spectroscopy is commonly used to characterize dipole orientation or
 168 molecular order given that the symmetry of the system is known. Recently, the uniaxial

169 symmetry of Na-SWy-3 clays was verified, enabling the calculation of the anisotropic optical
 170 constants [18]. For a beam propagating on the ATR crystal surface along the x direction, the
 171 evanescent field is directed normal to this surface in the z direction. Using p-polarized radiation,
 172 the evanescent electric field has components in the x and z directions, while for s-polarization,
 173 it has components only in the y direction. Therefore, the mean-squared amplitude of the electric
 174 field is separated into three orthogonal components:

$$175 \quad \langle E^2 \rangle = \langle E_x^2 \rangle + \langle E_y^2 \rangle + \langle E_z^2 \rangle \quad (1)$$

176 By using a projection similar to that for the electric field vector, μ , the vector representing the
 177 dipole change associated with a vibration, can be written as:

$$178 \quad \mu = \mu_x + \mu_y + \mu_z \quad (2)$$

179 To calculate the absorption intensity, the individual dipoles must be summed:

$$180 \quad A = \sum_i |\mu_i \cdot E|^2 \quad (3)$$

181 Making use of the polar angle as presented in **Figure 1a**, the absorbance can be written as:

$$182 \quad A_x = k \langle (\mu \cdot E_x)^2 \rangle = k \langle E_x^2 \rangle \sin^2(\theta) \cos^2(\phi) \quad (4a)$$

$$183 \quad A_y = k \langle (\mu \cdot E_y)^2 \rangle = k \langle E_y^2 \rangle \sin^2(\theta) \sin^2(\phi) \quad (4b)$$

$$184 \quad A_z = k \langle (\mu \cdot E_z)^2 \rangle = k \langle E_z^2 \rangle \cos^2(\theta) \quad (4c)$$

185 For transition moments that are axially distributed around the z axis, as is the case for clays, all
 186 values of ϕ are equiprobable:

$$187 \quad \langle \cos^2(\phi) \rangle = \langle \sin^2(\phi) \rangle = \frac{1}{2} \quad (5)$$

188 The dichroic ratio is obtained by dividing the p-polarized absorbance by the s-polarized
 189 absorbance:

$$190 \quad R_{ATR} = \frac{A_p}{A_s} = \frac{A_x + A_z}{A_y} = \frac{\langle E_x^2 \rangle \sin^2(\theta) + 2\langle E_z^2 \rangle \cos^2(\theta)}{\langle E_y^2 \rangle \sin^2(\theta)} \quad (6)$$

191 For any orientations of the dipole defining an isotropic system, the isotropic dichroic ratio is
 192 written as:

$$193 \quad R_{iso} = \frac{\langle E_x^2 \rangle + \langle E_z^2 \rangle}{\langle E_y^2 \rangle} \quad (7)$$

194 The order parameter S characterizing the degree of preferential orientation is calculated on the
 195 basis of 2nd-order Legendre polynomials as:

$$196 \quad S = \langle P_2 \cos(\theta) \rangle = \left\langle \frac{3}{2} \cos^2(\theta) - \frac{1}{2} \right\rangle \quad (8)$$

197 By substituting the angular factor in equation 8, the order parameter S is then defined as:

$$198 \quad S = \frac{\langle E_x^2 \rangle - R_{ATR} \langle E_y^2 \rangle + \langle E_z^2 \rangle}{\langle E_x^2 \rangle - R_{ATR} \langle E_y^2 \rangle - 2 \langle E_z^2 \rangle} \quad (9)$$

199 The S value can reach values from -0.5 to 1. A value of -0.5 indicates that all transition moments
 200 are precisely and uniformly oriented in the x or y direction, while a value of 1 indicates
 201 transition moments along the z axis. Values of 0 are obtained for isotropic materials, where all
 202 dipole moments have random orientation around the z axis or are all oriented at the magic angle
 203 ($\theta = 54.7^\circ$).

204 The evaluation of the order parameter requires the calculation of the electric field $\langle E^2 \rangle$. The
 205 general procedure for calculating the electric field amplitude at any point along a stratified
 206 system was developed by Hansen [21]. Here, only the analytical expression will be given for a
 207 3-phase system, as depicted in **Figure 1b** [32-34]. Because these expressions explicitly take
 208 into account the thickness and absorption properties of the sample, they are called thickness-
 209 and absorption-dependent equations:

210 -----

$$211 \quad \langle E_{y(j=1)}^2(z) \rangle = \left\{ (1 + R_s) + 2\sqrt{R_s} \cos \left(\delta^s - \frac{4\pi d \xi_1}{\lambda} \right) \right\} \quad (10a)$$

$$212 \quad \langle E_{y(j=2)}^2(z) \rangle = \left| (1 + r_s) \cos \left(\frac{2\pi d \xi_2}{\lambda} \right) + i \left(\frac{\xi_1}{\xi_2} \right) (1 - r_s) \sin \left(\frac{2\pi d \xi_2}{\lambda} \right) \right|^2 \quad (11a)$$

$$213 \quad \langle E_{y(j=3)}^2(z) \rangle = |t_s|^2 \exp \left(\frac{-4\pi \text{Im}(\xi_3)}{\lambda} \right) (z - d) \quad (12a)$$

214 -----

$$215 \quad \langle E_{x(j=1)}^2(z) \rangle = \cos^2(\alpha) \left\{ (1 + R_p) - 2\sqrt{R_p} \cos \left(\delta^p - \frac{4\pi d \xi_1}{\lambda} \right) \right\} \quad (10b)$$

216 $\langle E_{x(j=2)}^2(z) \rangle = \left| \cos(\alpha) (1 - r_p) \cos\left(\frac{2\pi d \xi_2}{\lambda}\right) + i \left(\frac{\xi_2 n_1}{\hat{n}_2^2}\right) (1 + r_p) \sin\left(\frac{2\pi d \xi_2}{\lambda}\right) \right|^2$ (11b)

217 $\langle E_{x(j=3)}^2(z) \rangle = \left| \frac{\xi_3}{\hat{n}_3} t_p \right|^2 \exp\left(\frac{-4\pi \text{Im}(\xi_3)}{\lambda}\right) (z - d)$ (12b)

218 -----

219 $\langle E_{z(j=1)}^2(z) \rangle = \sin^2(\alpha) \left\{ (1 + R_p) + 2\sqrt{R_p} \cos\left(\delta^p - \frac{4\pi d \xi_1}{\lambda}\right) \right\}$ (10c)

220 $\langle E_{z(j=2)}^2(z) \rangle = \left| \frac{n_1^2 \sin(\alpha)}{\hat{n}_2^2} (1 - r_p) \cos\left(\frac{2\pi d \xi_2}{\lambda}\right) + i \left(\frac{n_1 \sin(\alpha)}{\xi_2}\right) \cos(\alpha) (1 + r_p) \sin\left(\frac{2\pi d \xi_2}{\lambda}\right) \right|^2$

221 (11c)

222 $\langle E_{z(j=3)}^2(z) \rangle = \left| \frac{n_1 \sin(\alpha)}{\hat{n}_3} t_p \right|^2 \exp\left(\frac{-4\pi \text{Im}(\xi_3)}{\lambda}\right) (z - d)$ (12c)

223 where $\xi_j = \hat{n}_j \cos(\hat{\alpha}_j)$, j is the layer taking a value from 1 to 3 for a 3-phase system, \hat{n}_j is the
 224 isotropic complex optical constant ($\hat{n}_j = n_j + i\kappa_j$), α is the angle of incidence, R_s and R_p are
 225 the reflectance signals, and r_s , r_p , t_s and t_p correspond to the Fresnel coefficients calculated
 226 with the expressions given in [18].

227 Alternatively, Harrick proposed equations to calculate the amplitude of the electric field in the
 228 second phase of a 3-phase system when the film thickness is very large compared to the
 229 evanescent wave depth of penetration [35, 36]. In this approximation, the film is neglected, and
 230 **equations 11a-c** are resolved at $z = 0$ for $d = 0$ and $n_2 = 1$ (air). This corresponds to a 2-phase

231 system, and therefore, these approximations are referred to as the 2-phase approximations. This
 232 gives the following analytical expressions (**equation 13a-c**):

$$233 \quad \langle E_{y(j=2)}^2(z=0) \rangle = \frac{4 \cos^2(\alpha)}{1-n_{21}^2} \quad (13a)$$

$$234 \quad \langle E_{x(j=2)}^2(z=0) \rangle = \frac{4 \cos^2(\alpha)(\sin^2(\alpha)-n_{21}^2)}{(1-n_{21}^2)[(1+n_{21}^2)\sin^2(\alpha)-n_{21}^2]} \quad (13b)$$

$$235 \quad \langle E_{z(j=2)}^2(z=0) \rangle = \frac{4 \cos^2(\alpha)\sin^2(\alpha)}{(1-n_{21}^2)[(1+n_{21}^2)\sin^2(\alpha)-n_{21}^2]} \quad (13c)$$

236 where $n_{21} = n_2/n_1$, with n_1 and n_2 being the real parts of the refractive indexes of phases 1
 237 and 2, respectively.

238 In the other extreme case, where the film is very small compared to the penetration depth of the
 239 evanescent wave, the electric field amplitude in the second phase can be calculated from
 240 **equations 11a-c** at $z = 0$ by setting $d = 0$ and $n_2 = n_{\text{film}}$. In this approximation, the film is
 241 optically considered but treated as non-absorbing ($\kappa_2 = 0$), and the following analytical
 242 equations are referred to as the thin-film approximation:

$$243 \quad \langle E_{y(j=2)}^2(z=0) \rangle = \frac{4 \cos^2(\alpha)}{1-n_{31}^2} \quad (14a)$$

$$244 \quad \langle E_{x(j=2)}^2(z=0) \rangle = \frac{4 \cos^2(\alpha)(\sin^2(\alpha)-n_{31}^2)}{(1-n_{31}^2)[(1+n_{31}^2)\sin^2(\alpha)-n_{31}^2]} \quad (14b)$$

$$245 \quad \langle E_{z(j=2)}^2(z=0) \rangle = \frac{4 n_{32}^4 \cos^2(\alpha)\sin^2(\alpha)}{(1-n_{31}^2)[(1+n_{31}^2)\sin^2(\alpha)-n_{31}^2]} \quad (14c)$$

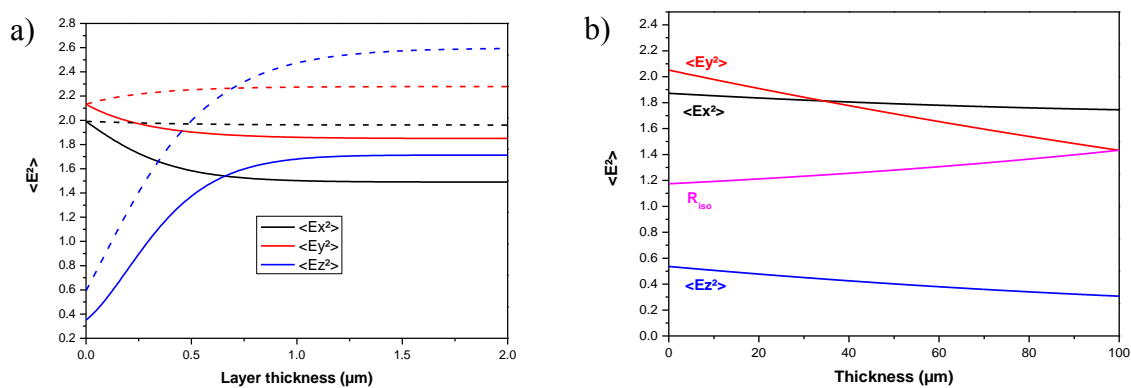
246 where $n_{31} = n_3/n_1$ and $n_{32} = n_3/n_2$

247 **IV. Results and Discussion**

248 **IV.1. Electric field propagation within a clay sample deposited on a Ge ATR crystal**

249 The availability of rigorous mathematical treatments for determining electric field propagation
250 through a sample enables a better understanding of the origin of ATR band intensity [21]. The
251 macroscopic treatment of the electric field considers interfaces between two media as a step
252 function of their respective dielectric constants [37-39]. Implicitly, the macroscopic physical
253 properties of a layer are assumed to be adequate descriptors of their microscopic properties,
254 irrespective of their dimensions or chemical/physical environments. As a consequence,
255 electromagnetic field theory accurately describes the electric field amplitude within a few
256 angstroms from the surface. Although the expressions are mathematically exact, they are not
257 exact in the sense of physics for describing the electric field amplitude within a film whose
258 thickness is in the nanometer range. For this reason, it is not surprising to note that for similar
259 systems, some authors may use the thin-film set of equations, while others prefer the 2-phase
260 expressions [32, 40-45]. This illustrates well that profound differences exist in the way that
261 authors use theory to interpret the molecular orientation of thin films. Interestingly, Citra and
262 Axelsen, for example, demonstrate that contrary to expectations, the 2-phase approximation is
263 more appropriate for describing a 25-50 Å thick layer of phospholipids [45]. Considering the
264 above arguments, it is surprising that very little attention has been paid to determining which
265 set of expressions is more appropriate and accurate for given experimental conditions.

266 It is therefore of interest to evaluate the various theoretical treatments given above by carefully
267 examining the plausibility of the order parameter as obtained. More specifically, constraints
268 having the ability to dismiss a given approach if the results are irrelevant must be added. This
269 methodology offers advantages in understanding the origin of failures in theory. For example,
270 if the 2-phase system adequately describes the molecular orientation, it suggests that the optical
271 properties of the thin film are best ignored. Although questionable in terms of physics, it is
272 certainly more reasonable than systematically employing thin-film expressions when thin films
273 are deposited on an ATR crystal. This mismatch between theory and experiment originates from
274 the inherent difficulty of optically describing a thin film layer. Modifications of the dielectric
275 functions at the interface accounting for surface rugosity may substantially influence the electric
276 field amplitude within the thin film. Using an effective dielectric constant may partially solve
277 the problem, even if difficulties in experimentally determining this effective dielectric function
278 of a very thin layer still subsist [46]. Anderson and Hansen calculated the electric field
279 amplitude of an idealized single film composed of multiple anisotropic layers and showed that
280 optical constants may be chosen to reflect the physical behavior of the interface. This approach
281 assimilates optical constants not as a bulk phase optical property but rather as arbitrary fitting
282 parameters [47].



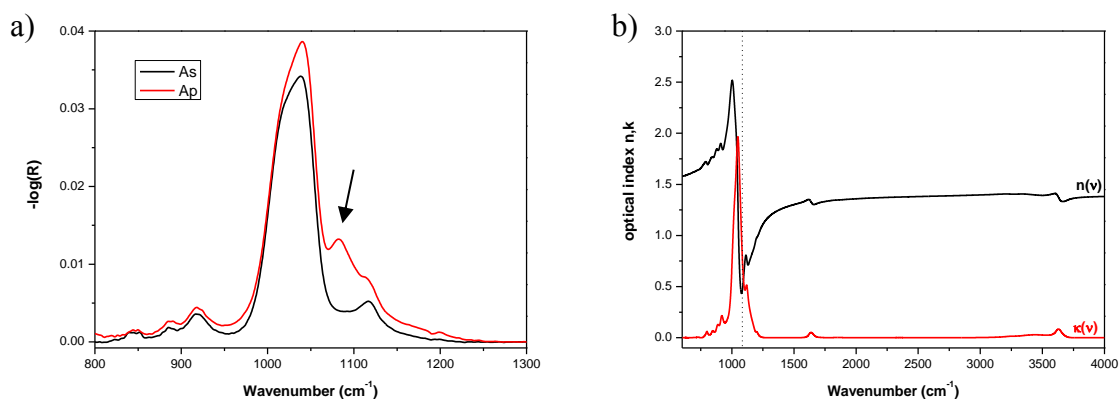
283
 284 **Figure 2.** Orthogonal mean squared electric field amplitude a) at the interface between Ge IRE
 285 and a clay film as a function of the film thickness for absorbing (plain line) and non-absorbing
 286 (dashed line) films and b) along the thickness of a 100 nm thick film.

287 In **Figure 2a**, the electric field amplitudes along the x, y and z axes were calculated using the
 288 thickness- and absorption-dependent equations for an isotropic 3-phase system (Ge IRE – Clay
 289 – Air; **Figure 1b**). The calculations were performed with an assumption of isotropic refractive
 290 indexes of 4 for Ge IRE, 1.4 for the clay film and 1 for air at 1085 cm^{-1} and an incidence angle
 291 of 45° . The three orthogonal components were computed at the interface between the ATR
 292 crystal and the clay film for different thicknesses of the clay film. The clay film was treated as
 293 a non-absorbing ($k = 0$) and absorbing ($k = 0.7675$) medium. Among the three orthogonal
 294 components of the electric field, $\langle E_z^2 \rangle$ exhibits the largest variation, with values ranging from
 295 0.350 and 0.592 to 1.712 and 2.593 for a $2\text{ }\mu\text{m}$ thick film for absorbing and non-absorbing
 296 media, respectively (**Figure 2a**). In the same thickness range, $\langle E_x^2 \rangle$ and $\langle E_y^2 \rangle$ show only a
 297 slight variation, which is more pronounced for absorbing media, where an overall decrease in
 298 the amplitude is observed compared to that in a non-absorbing medium. The thin-film and 2-

299 phase approximations correspond to the amplitudes at which the thicknesses are 0 and 2 μm ,
300 respectively, for the non-absorbing media. For the absorbing medium, these approximations
301 give values closer to the exact calculations for very thin films than for thick films. Difficulties
302 arise for intermediate film thicknesses of up to 1 μm , where the two approximate sets of
303 equations do not allow a reliable estimation of the electric field components. Therefore,
304 neglecting the imaginary part of the complex optical constants can induce significant variations
305 in the computation of electric field amplitude, leading to an erroneous determination of order
306 parameter S.

307 In **Figure 2b**, the evolution of the electric field amplitude along the thickness for a 100 nm
308 thick film is shown. The electric field components are not constant within the film and decrease
309 almost linearly. The isotropic ratio, R_{iso} , increases when the film thickness increases, illustrating
310 the inherent uncertainty when the calculations are performed only at the interface between the
311 ATR crystal and the film. Therefore, the thinner the film is, the more accurate the determination
312 of the molecular orientation. Nevertheless, a mean value of the three orthogonal components of
313 the electric field within the film thickness is preferred to achieve more reliable results [44].

314 **IV.2. Optical constants and definition of the order parameters S for the Na-SWy-3**
315 **film.**



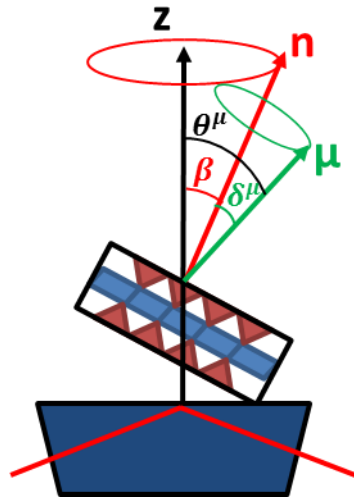
316

317 **Figure 3.** a) Experimental s- and p-polarized spectra of a 22 nm thick Na-SWy-3 film on Ge
 318 IRE and b) isotropic optical constants, $n(\nu)$ and $\kappa(\nu)$, of Na-SWy-3 from [18].

319 **Figure 3a** presents the ATR spectra of the 22 nm thick film analyzed with s- and p-polarization.
 320 The most obvious change is the increase in the band located at 1085 cm^{-1} assigned to a
 321 longitudinal mode with a transition moment oriented perpendicular to the film plane involving
 322 stretching vibrations between Si and the apical oxygen of the tetrahedron, Si-O_{ap}. Recalling
 323 that the magnitude of light absorption depends on the mutual orientation of the vectors
 324 associated with the transition moment and the electric field, the determination of the order
 325 parameter provides insight into the orientation of the dipole moment with respect to the normal
 326 to the interface. As a consequence, the determination of the orientation of the normal to the clay
 327 film with respect to the z axis requires the determination of the orientation of the dipole moment
 328 with respect to the normal to the clay layer. In the following, the transition moment associated
 329 with the vibration at 1085 cm^{-1} is assumed to be colinear with the Si-O_{ap} bond. This transition
 330 moment is inclined by an angle δ with respect to the normal of the clay layer and isotropically
 331 distributed around it. Furthermore, the normal to the clay layer forms an angle β with the z axis

332 and is isotropically distributed around it (**Figure 4**). The order parameter measured from the
 333 ATR dichroic ratio can be expressed as a superposition of two uniaxial orientations according
 334 to:

335
$$S_{\theta}^{SiO} = S_{\beta} \cdot S_{\delta}^{SiO} \quad (15)$$



336
 337 **Figure 4.** Geometric representation of the axially symmetric distribution of orientation of the
 338 transition moment μ around the normal to the clay layer n (angle δ), which is distributed around
 339 the reference direction, z (angle β). The distribution of the transition moment around the z axis
 340 is characterized by the angle θ

341 **IV.3. Experimental determination of S_{δ}^{SiO} from a single layer deposit**

342 In the limit case where a single layer of smectite is deposited on the ATR crystal (S_{β} is assumed
 343 to be equal to 1), **equation 15** is reduced to $S_{\theta}^{SiO} = S_{\delta}^{SiO}$, offering the possibility to determine

344 the angle between the transition moment under investigation and the normal to the clay surface.
345 Such an experiment can be achieved with the Langmuir-Blodgett technique, as performed by
346 *Ras et al.* [19] This film preparation technique generally leads to a higher degree of organization
347 than the layer-by-layer assembly (LbL) because in the former case, the film is formed at the
348 gas/liquid interface and offers additional control on the lateral distribution of clay mineral
349 particles [19, 48]. Although previous experiments were performed on Na-SWy-1, we assumed
350 that the optical constants that were previously determined for Na-SWy-3 are valid [18]. The
351 dichroic ratio measured by these authors on a unique layer of Na-SWy-1 was found to be 8.33
352 using a ZnSe IRE. Based on the extraction of the isotropic optical constants from **Figure 3b** at
353 1085 cm^{-1} ($n_2 = 0.467$; $\kappa_2 = 0.768$), the mean square electric field amplitudes were calculated
354 using the different sets of equations presented in the theory section (**Table 1a**). For the three
355 sets of equations, similar results were obtained for the calculations of $\langle E_x^2 \rangle$ and $\langle E_y^2 \rangle$,
356 whereas important variations were noted for $\langle E_z^2 \rangle$. Given the very thin thickness of the sample,
357 the difference observed between the thin-film approximation and the thickness- and absorption-
358 dependent equations originates from the attenuation coefficient, which drastically reduced the
359 $\langle E_z^2 \rangle$ value from 61.55 to 4.49. This last value is close to that calculated with the 2-phase
360 approximation, where the film is not considered. The order parameter S_θ^{SiO} , which is strongly
361 influenced by the value of $\langle E_z^2 \rangle$ according to **equation 9**, was also calculated, as shown in
362 **Table 1a**, along with the $\langle \theta \rangle$ value, assuming that $\langle \cos^2(\theta) \rangle = \cos^2(\langle \theta \rangle)$, which
363 holds only for a very narrow distribution of θ . The value of $\langle \theta \rangle$ calculated using the thin-film
364 approximations is irrelevant since it would signify that the transition moment is directed within
365 the plane of the clay layer. For the other equations used to compute the electric field amplitude,
366 $\langle \theta \rangle$ values of 30° and 35° were obtained. In that case, the tilt angles appear to be very large,

367 which would suggest large deformations of the tetrahedral units, which is contradictory to the
 368 XRD analysis and molecular dynamics simulations [49-52]. Therefore, using the as-determined
 369 optical indexes, none of the equations for the calculations of the mean square electric field
 370 amplitudes is reliable. This suggests that the electromagnetic theory fails to properly describe
 371 thin films of clay deposited on ATR crystals.

372 **Table 1.** Values of the three orthogonal mean square electric field amplitudes at 1085 cm⁻¹
 373 calculated using the formalisms presented in the theory section, the order parameter of the
 374 transition moment and the tilt angle.

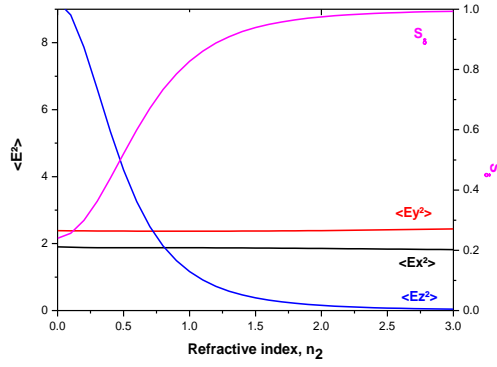
375

	$\langle E_x^2 \rangle$	$\langle E_y^2 \rangle$	$\langle E_z^2 \rangle$	S_θ^{SiO}	$\langle \theta^{SiO} \rangle^d$
a) Na-SWy – $n_1 = 2.41$; $n_2 = 0.467$; $R_{ATR} = 8.33^e$; $\nu = 1085 \text{ cm}^{-1}$					
Thin Film ^a - $\kappa_2 = 0$; $d = 0 \text{ nm}$	1.914	2.416	61.547	-0.307	69°
2-phase approximation ^b $\kappa_2 = 0$; $d > d_p$	1.914	2.416	2.917	0.636	30°
Thickness-Absorption dependent ^c $\kappa_2 = 0.768$; $d = 1 \text{ nm}$	1.914	2.411	4.488	0.504	35°
b) Na-SWy – $n_1 = 2.41$; $n_2 = 1.40$; $R_{ATR} = 8.33^e$; $\nu = 1085 \text{ cm}^{-1}$					
Thin Film - $\kappa_2 = 0$; $d = 0 \text{ nm}$	1.914	2.416	0.759	0.885	16°
2-phase approximation $\kappa_2 = 0$; $d > d_p$	1.914	2.416	2.917	0.636	30°
Thickness-Absorption dependent $\kappa_2 = 0.768$; $d = 1 \text{ nm}$	1.912	2.411	0.449	0.929	13°
c) Na-SWy – $n_1 = 4$; $n_2 = 1.40$; $R_{ATR} = 4.10$; $\nu = 1085 \text{ cm}^{-1}$					
Thin Film - $\kappa_2 = 0$; $d = 0 \text{ nm}$	1.991	2.133	0.592	0.776	23°

2-phase approximation $\kappa_2 = 0; d > d_p$	1.991	2.133	2.276	0.396	39°
Thickness-Absorption dependent $\kappa_2 = 0.768; d = 22 \text{ nm}$	1.954	2.031	0.362	0.847	19°

376 a Assuming an infinite and non-absorbing thin film - see equation 14a-c
377 b The film is not considered – see equation 13a-c
378 c The electric field amplitude is averaged over the film thickness - see equation 11a-c
379 d Assuming an infinitely narrow orientational distribution $\langle \cos^2(\theta) \rangle = \cos^2(\langle \theta \rangle)$
380 e R_{ATR} taken from refs [19, 48]. Note that the authors in these references expressed the dichroic ratio as A_p/A_s and
381 was converted to be consistent with our definition - see equation 6.
382

383 To overcome this difficulty, we analyzed the order parameter S_δ^{SiO} as a function of the isotropic
384 value of the refractive index of the clay film (**Figure 5**). The extinction coefficient, $\kappa(\nu)$, which
385 represents the dynamic dipole moment and describes the absorption of the electromagnetic
386 radiation, was set to 0.768 [53, 54]. Although the values of $\langle Ex^2 \rangle$ and $\langle Ey^2 \rangle$ seem insensitive
387 to the refractive index, n_2 , drastic variation in $\langle Ez^2 \rangle$ is noted, which in turn affects the calculated
388 S_δ^{SiO} value. Changes in S_δ^{SiO} are the most important for the n_2 value in the range of 0–1 and
389 correspond to less than 2% of the variation per 0.1 unit of refractive index above $n_2 = 1.4$. The
390 determination of the refractive index value is therefore of prime importance and strongly affects
391 the determination of the particle orientations. For these out-of-plane Si-O stretching vibrations,
392 values of n_2 between 0.61 and 1.15 have been reported for Na-SWy layers that lead to strongly
393 different order parameters [19, 20, 55].



394

395 **Figure 5.** Evolution of the mean square electric field amplitude calculated with equation 11a-c
 396 and the order parameter as a function of the refractive index of a Na-SWy-3 single layer ($d = 1$
 397 nm) on ZnSe IRE. The input parameters are $R_{ATR} = 8.33$, $\nu = 1085 \text{ cm}^{-1}$ and $\kappa_2 = 0.768$.

398 To obtain more insight into the maximum value of S_δ^{SiO} , MD simulations were performed on a
 399 montmorillonite layer. The angle between the Si-O apical bond and the normal to the clay layer
 400 was extracted and averaged over a simulation period of 125 fs. Subsequently, the distribution
 401 function $f(\delta)$ was extracted, and the $S_\delta^{SiO}(MD)$ value was calculated according to:

$$402 \quad S_\delta^{SiO} = \langle P_2 \cos(\delta) \rangle = \left\langle \frac{3}{2} \cos^2(\delta) - \frac{1}{2} \right\rangle \quad (16)$$

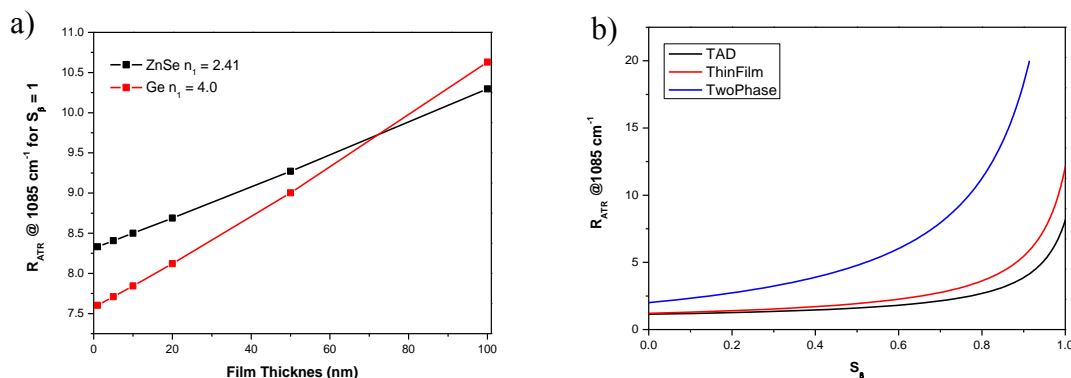
403 The $S_\delta^{SiO}(MD)$ value obtained was 0.987, corresponding to a $\langle \delta \rangle$ value of 5.33° . Reporting this
 404 value in **Figure 5** enables determination of a refractive index value of 2.4. Since this value is
 405 extracted on the basis of structural considerations from molecular simulations, it has to be
 406 regarded as the maximum value relating the transition moment to the normal of the clays.
 407 Submicron natural clay minerals may present structural faults and layer flexibility, leading to a

408 more disordered structure that would in turn decrease the experimental S_{δ}^{SiO} value [56, 57]. Due
409 to the inherent difficulty in precisely determining this value and given the low intensity of the
410 1085 cm^{-1} ATR band, an arbitrary value of refractive index of 1.4 will be used, resulting in an
411 S_{δ}^{SiO} value of 0.929 (**Table 1b**). This corresponds to the refractive index in a region where there
412 is no absorption in **Figure 3b** and may indicate that the experimental value of 0.467 for n_2 is
413 decreased substantially by the strong anomalous dispersion associated with the very intense Si-
414 O stretching vibration at 1039 cm^{-1} .

415 **IV.4. Experimental determination of S_{β} for thin film deposits**

416 For the 22 nm thick Na-SWy-3 deposit on the Ge IRE, an experimental dichroic ratio of 4.1
417 was measured. Using the newly determined value of the refractive index, the electric field
418 amplitudes were calculated with the approximate and exact equations (**Table 1c**). Both thin-
419 film approximations and thickness- and absorption-dependent equations give similar S_{θ}^{SiO}
420 values of 0.776 and 0.847, respectively, while a value of 0.396 was obtained using the 2-phase
421 approximations. This suggests that the optical properties of the clay film have to be taken into
422 account for reliable calculation of the electric field amplitude. Using **equation 15** and the
423 calculated value of S_{δ}^{SiO} (0.929), the order parameter representing the orientation of the normal
424 to the clay film with respect to the z axis, S_{β} , is 0.912, corresponding to a $\langle\beta\rangle$ value of 14°. In
425 a recent publication, measurements of the order parameters of a dozen-micrometer-thick Na-
426 SWy-2 film led to an experimental S_{β} value of approximately 0.65 [58]. For thinner sample
427 preparation, as used for FTIR spectroscopy measurements, a higher S_{β} value would be
428 expected, accounting for the lower number of layers investigated and their less disordered

429 organization. Therefore, our results are consistent and fully support the determined value of
 430 S_{δ}^{SiO} .



431
 432 **Figure 6.** a) Evolution of the dichroic ratio for different film thicknesses in the case of perfectly
 433 oriented Na-SWy-3 clay ($S_{\beta} = 1$) and b) expected dichroic ratio for various values of S_{β} obtained
 434 through the three sets of electric field amplitude calculations for a 20 nm thick film on Ge IRE.
 435 The input parameters are $\nu = 1085 \text{ cm}^{-1}$, $n_1 = 4$, $n_2 = 1.4$ and $\kappa_2 = 0.768$.

436 **Figure 6a** presents the variation in the dichroic ratio as a function of the sample thickness for
 437 the 1085 cm^{-1} band and considering $S_{\beta} = 1$. The nature of the ATR IRE element dictates the
 438 value of the dichroic ratio as measured irrespective of the particle organization. Upon variation
 439 of the sample thickness, a sharper increase is observed with the Ge IRE than with the ZnSe or
 440 diamond IRE. Therefore, reliable orientation measurements require the precise determination
 441 of the sample thickness. As a consequence, a comparison of the dichroic ratio can be performed
 442 only with similar IRE elements. **Figure 6b** presents the influence of S_{β} on the dichroic ratio
 443 measured on the 22 nm film with a Ge IRE using different formalisms for the calculations of
 444 the electric field. Regarding the results obtained from the thickness- and absorption-dependent

445 equations, the variation in the dichroic ratio for S_β below 0.6 is very limited. This suggests that
446 precise orientation measurements of nearly isotropic clay particles may not be achievable using
447 ATR spectroscopy. In this case, other transition moments should be considered. **Figure 6b** also
448 suggests the need to determine the dichroic ratio with the best accuracy. The highest precision
449 of the orientation measurement was achieved for S_β greater than 0.6, where large variations in
450 the dichroic ratio were correlated to small variations in the clay orientation. It can thus be
451 concluded that the orientation of an anisotropic clay particle organization can readily be
452 determined using ATR-FTIR spectroscopy according to the methodology proposed here.
453 Moreover, using the approximate equations instead of the most complete equations may
454 underestimate the S_β value. Future directions for this work could be the experimental
455 determination of the orientation of all transition moments of clays with respect to the clay
456 normal, but the validity of the assumptions for the electric field calculations still need to be
457 proven.

458 **IV.5. Determination of structural hydroxyl and interlayer water orientations with** 459 **respect to the clay layer surface.**

460 The benefit of ATR-FTIR spectroscopy lies in its high sensitivity for probing interfacial
461 phenomena. For a more accurate description of the organization of organic molecules on
462 mineral surfaces, from the nanometer to the micrometer scales, the mineral organization must
463 be taken into account. This is illustrated in this section, where the orientations of structural
464 hydroxyls and water molecules are determined with respect to the clay mineral surface, which
465 allows comparison with the MD results.

466 To improve the signal-to-noise ratio, spectra were calculated from the anisotropic optical
 467 constants determined on a thick deposit of Na-SWy-3 (>2 μm). Subsequently, s- and p-
 468 polarized ATR spectra were computed assuming a 1 nm thin film, where the information about
 469 the orientation of all transition moments corresponds to that of the bulk deposit. This procedure
 470 guarantees a high-quality spectrum with an improved signal-to-noise ratio. The normal to the
 471 clay orientation with respect to the z axis was determined from the Si-O stretching vibration
 472 dichroic ratio at 1085 cm^{-1} according to the method described in this paper. The clay mineral
 473 hydroxyl orientation was determined from their stretching vibrations at 3630 cm^{-1} . Due to the
 474 strong overlap between the vibrations of hydroxyl groups and those of water, the same thick
 475 deposit was dehydrated under an air-dried stream for 24 h, and the dehydrated-clay optical
 476 constants were extracted for the simulation of polarized ATR spectra. Using dehydrated or
 477 monohydrated samples was not observed to significantly affect the experimental dichroic ratio
 478 of the Si-O stretching bands, so the orientation of the particles remained equivalent for both
 479 hydration states, in agreement with the MD simulations. For water molecules, the dichroic ratio
 480 from the bending motion at 1637 cm^{-1} was calculated. For both transition moments, the uniaxial
 481 orientation of the transition moment was determined with respect to the z axis (S_{θ}^{OH}). To discard
 482 the influence of particle orientations, an order parameter relative to the normal to the clay, S_{δ}^{OH} ,
 483 was obtained according to:

$$484 \quad S_{\delta}^{OH \text{ or } H_2O} = \frac{S_{\theta}^{OH \text{ or } H_2O}}{S_{\beta}} \quad (17)$$

485 where S_{β} is determined using **equation 15**. The dichroic ratio of the SiO stretching vibrations
 486 extracted from the simulated s- and p-polarized spectra was found to be 2.77, corresponding to

487 a S_β value of 0.847. This value is lower than that measured for a 22 nm thick sample ($S_\beta =$
488 0.912), suggesting slightly less anisotropic particle organization for thicker deposits (**Table**
489 **2a**). Using the isotropic optical constants from **Figure 3b** at the wavenumbers of the two
490 transition moments, i.e., 3630 cm^{-1} and 1638 cm^{-1} for $\nu_{\text{MO-H}}$ and δ_{HOH} , respectively, and the
491 experimentally determined dichroic ratio, the order parameter S_θ^{OH} was calculated according to
492 **equation 9** and converted to S_δ^{OH} using **equation 17**. MD simulations were comparatively
493 performed, and the angular distributions of the transition moments were extracted and are
494 reported in **Table 2b-c**. The structural hydroxyls give an experimental S_δ^{OH} value of -0.421,
495 which is very close to that determined by MD simulations (-0.436), confirming that the
496 hydroxyls are oriented nearly parallel to the layer, as expected for dioctahedral smectites. The
497 good agreement between the experimental and expected S_δ^{OH} values fully supports the
498 methodology presented in this work for extracting S_β and therefore validates the proposed
499 values of the optical constants, n_2 and κ_2 , to determine clay mineral orientation. The dichroism
500 ratio determined from the bending vibrations of the water molecules was 1.23, corresponding
501 to an $S_\delta^{\text{H}_2\text{O}}$ of -0.053. This value indicates that the orientation of the water molecules is nearly
502 isotropic. The MD-extracted value is slightly lower than the experimental value, reflecting a
503 higher proportion of water molecules with their dynamic transition moments perpendicular to
504 the z-axis. This slight discrepancy may originate from the contribution of surface-adsorbed
505 water molecules and/or 2W layers, as commonly observed at ambient humidity and not taken
506 into account in the simulations. [13, 30, 59]. On the basis of the MD simulations, *Szczerba et*
507 *al.* showed that 2W montmorillonite layers contain a higher proportion of bidentate water

508 molecules whose transition moments are parallel to the z axis, contributing to an increase in the
 509 $S_{\delta}^{H_2O}$ value [60].

510 **Table 2:** Determination of the order parameters S_{β} , S_{θ}^{μ} and S_{δ}^{μ} using the thickness- and
 511 absorption-dependent equations and comparison with the MD results

	S_{β}	S_{θ}^{OH}	S_{δ}^{OH} or $S_{\delta}^{H_2O}$	$\langle \delta^{OH} \rangle$ or $\langle \delta^{H_2O} \rangle$	S_{δ}^{OH} or $S_{\delta}^{H_2O}$ from MD
a) ν_{SiO} – $n_1 = 4$; $n_2 = 1.4$; $\kappa_2 = 0.768$; $R_{ATR} = 2.77$; $\nu = 1085 \text{ cm}^{-1}$; $d = 1 \text{ nm}$					
Thickness-Absorption dependent	0.847	x	x	x	x
b) ν_{MO-H} – $n_1 = 4$; $n_2 = 1.388$; $\kappa_2 = 0.033$; $R_{ATR} = 1.01$; $\nu = 3630 \text{ cm}^{-1}$; $d = 1 \text{ nm}$					
Thickness-Absorption dependent	0.847	-0.356	-0.421	77°	[-0.437;-0.367] ^a
c) δ_{OH-O} – $n_1 = 4$; $n_2 = 1.330$; $\kappa_2 = 0.048$; $R_{ATR} = 1.23$; $\nu = 1638 \text{ cm}^{-1}$; $d = 1 \text{ nm}$					
Thickness-Absorption dependent	0.847	-0.045	-0.053	57°	[-0.213;-0.140] ^a

512
 513 a Extremum values from MD simulation assuming rigid or flexible clay
 514

515 V. Concluding remarks and perspectives

516 The present study provides the general methodology for determining clay particle orientation
 517 using polarized ATR-FTIR spectroscopy and allows the derivation of three major conclusions.
 518 First, Si-O_{ap} transition moments are suitable for determining clay particle orientations of rather
 519 anisotropic organizations ($S > 0.6$). The appropriate optical constants associated to the Si-O_{ap}
 520 vibration for reliable measurements of particle orientations were determined: the frequency
 521 dependence variation of the refractive index is best ignored (n_2 set to 1.4), and the extinction

522 coefficient was determined by pATR measurements to be $\kappa_2 = 0.768$. Second, by comparison
523 with the absorption- and thickness-dependent equations, the thin-film approximations often
524 used in literature [19, 61] were observed to slightly underestimate the order parameter, while
525 the 2-phase approximation yielded unreliable results. Third, as a proof of concept in the present
526 study, structural hydroxyl and water molecule orientations were experimentally determined on
527 Na-SWy-3 smectite with respect to the normal of the clay using equation 15 with an S_δ^{SiO} value
528 of 0.929 (which depends on the ATR IRE and the clay mineral studied) to extract S_β and
529 equation 17 to determine $S_\delta^{OH \text{ or } H_2O}$. This result was found to be in fairly good agreement with
530 the results of molecular dynamics simulations.

531 The present work extends the quantitative treatment of clay minerals using pATR methods to
532 include sample thicknesses larger than a single monolayer of particles [19, 48, 61]. This upper
533 scale, which could be referred as to the aggregate scale, is of particular importance for enabling
534 connection between the orientation of particles and the macroscopic properties of hybrid or
535 composite materials. Taking advantage of a reference function describing the orientation of clay
536 particles [62], the order parameter as obtained from pATR measurements using the presented
537 methodology is thus sufficient to determine the full shape of the orientation distribution
538 function. Such an information is a key parameter for the design of clay-based engineered
539 materials with tunable properties [63-66]. In addition to the refined analysis of clay particles
540 orientation by pATR measurements, the logical perspective of this work is to follow up this
541 study with orientation determination of organic molecules adsorbed on or intercalated within
542 clay particles. Because of the great sensitivity of FTIR spectroscopy to organic functional
543 groups, such investigation should help to identify how organic molecules interact with clay

544 interfaces. This is of particular importance given the prominent role played by organo-clays in
545 various applications.

546 **Acknowledgments**

547 The CNRS interdisciplinary “défi Needs”, through its “MiPor” program (Project
548 TRANSREAC), is acknowledged for providing financial support for this study. The authors
549 acknowledge financial support from the European Union (ERDF) and "Région Nouvelle
550 Aquitaine".

551

- 553 [1] W. Wang, A. Wang, Nanoscale Clay Minerals for Functional Ecomaterials: Fabrication,
554 Applications, and Future Trends, in: L.M.T. Martínez, O.V. Kharissova, B.I. Kharisov (Eds.),
555 Handbook of Ecomaterials, Springer International Publishing, Cham, 2019, pp. 2409-2490.
556 https://doi.org/10.1007/978-3-319-68255-6_125.
- 557 [2] M.I. Carretero, Clay minerals and their beneficial effects upon human health. A review,
558 Applied Clay Science 21(3) (2002) 155-163. [https://doi.org/10.1016/S0169-1317\(01\)00085-0](https://doi.org/10.1016/S0169-1317(01)00085-0).
- 559 [3] C.H. Zhou, An overview on strategies towards clay-based designer catalysts for green and
560 sustainable catalysis, Applied Clay Science 53(2) (2011) 87-96.
561 <https://doi.org/10.1016/j.clay.2011.04.016>.
- 562 [4] S.-J. Choi, Y.-R. Kim, Bioinspired Layered Nanoclays for Nutraceutical Delivery System,
563 Advances in Applied Nanotechnology for Agriculture, American Chemical Society 2013, pp.
564 207-220. <https://doi.org/10.1021/bk-2013-1143.ch012>.
- 565 [5] J. Ma, Q. Liu, L. Zhu, J. Zou, K. Wang, M. Yang, S. Komarneni, Visible light photocatalytic
566 activity enhancement of Ag₃PO₄ dispersed on exfoliated bentonite for degradation of
567 rhodamine B, Applied Catalysis B: Environmental 182 (2016) 26-32.
568 <https://doi.org/10.1016/j.apcatb.2015.09.004>.
- 569 [6] M. Ogawa, K. Kuroda, Photofunctions of Intercalation Compounds, Chemical Reviews
570 95(2) (1995) 399-438. <https://doi.org/10.1021/cr00034a005>.
- 571 [7] M.F. Brigatti, E. Galán, B.K.G. Theng, Chapter 2 - Structure and Mineralogy of Clay
572 Minerals, in: F. Bergaya, G. Lagaly (Eds.), Developments in Clay Science, Elsevier 2013, pp.
573 21-81. <https://doi.org/10.1016/B978-0-08-098258-8.00002-X>.
- 574 [8] M. Darder, M. López-Blanco, P. Aranda, F. Leroux, E. Ruiz-Hitzky, Bio-Nanocomposites
575 Based on Layered Double Hydroxides, Chem. Mater. 17(8) (2005) 1969-1977.
576 <https://doi.org/10.1021/cm0483240>.
- 577 [9] B. Wicklein, M. Darder, P. Aranda, E. Ruiz-Hitzky, Bio-organoclays based on
578 phospholipids as immobilization hosts for biological species, Langmuir 26(7) (2010) 5217-
579 5225. <https://doi.org/10.1021/la9036925>.
- 580 [10] J.W. Jordan, Organophilic Bentonites. I. Swelling in Organic Liquids, The Journal of
581 Physical and Colloid Chemistry 53(2) (1949) 294-306. <https://doi.org/10.1021/j150467a009>.
- 582 [11] A. Yamagishi, M. Soma, Optical resolution of metal chelates by use of adsorption on a
583 colloidal clay, Journal of the American Chemical Society 103(15) (1981) 4640-4642.
584 <https://doi.org/10.1021/ja00405a086>.
- 585 [12] M. Eguchi, T. Shimada, D.A. Tryk, H. Inoue, S. Takagi, Role of Hydrophobic Interaction
586 in Controlling the Orientation of Dicationic Porphyrins on Solid Surfaces, The Journal of
587 Physical Chemistry C 117(18) (2013) 9245-9251. <https://doi.org/10.1021/jp400645d>.
- 588 [13] E. Ferrage, B. Lanson, B.A. Sakharov, V.A. Drits, Investigation of smectite hydration
589 properties by modeling experimental X-ray diffraction patterns: Part I. Montmorillonite
590 hydration properties, American Mineralogist 90(8-9) (2005) 1358.
591 <https://doi.org/10.2138/am.2005.1776>.
- 592 [14] F. Hubert, D. Prêt, E. Tertre, E. Ferrage, B. Nauleau, I. Bihannic, M. Pelletier, B. Demé,
593 Investigating the anisotropic features of particle orientation in synthetic swelling clay porous

594 media, Clays and Clay Minerals 61(5) (2013) 397-415.
595 <https://doi.org/10.1346/ccmn.2013.0610501>.

596 [15] E. Ferrage, F. Hubert, A. Baronnet, O. Grauby, E. Tertre, A. Delville, I. Bihannic, D. Pret,
597 L.J. Michot, P. Levitz, Influence of crystal structure defects on the small-angle neutron
598 scattering/diffraction patterns of clay-rich porous media, *Journal of Applied Crystallography*
599 51(5) (2018) 1311-1322. <https://doi.org/10.1107/S160057671801052X>.

600 [16] T. Dabat, A. Mazurier, F. Hubert, E. Tertre, B. Grégoire, B. Dazas, E. Ferrage, Mesoscale
601 Anisotropy in Porous Media Made of Clay Minerals. A Numerical Study Constrained by
602 Experimental Data, *Materials* 11(10) (2018). <https://doi.org/10.3390/ma11101972>.

603 [17] R. Ikeda, B. Chase, N.J. Everall, Basics of Orientation Measurements in Infrared and
604 Raman Spectroscopy, in: M. Chalmers, P.R. Griffiths (Eds.), *Handbook of Vibrational*
605 *Spectroscopy* 2001. <https://doi.org/10.1002/9780470027325.s0501m.pub2>.

606 [18] B. Grégoire, B. Dazas, M. Leloup, F. Hubert, E. Tertre, E. Ferrage, S. Petit, Optical theory
607 based simulation of Attenuated Total Reflection infrared spectra of Montmorillonite, Submitted
608 to *Clays and Clay Minerals* (2019).

609 [19] R.H.A. Ras, C.T. Johnston, E.I. Franses, R. Ramaekers, G. Maes, P. Foubert, F.C. De
610 Schryver, R.A. Schoonheydt, Polarized Infrared Study of Hybrid Langmuir–Blodgett
611 Monolayers Containing Clay Mineral Nanoparticles, *Langmuir* 19(10) (2003) 4295-4302.
612 <https://doi.org/10.1021/la026786r>.

613 [20] A. Holmgren, X. Yang, A Polarized Fourier Transform Infrared Spectrometry Attenuated
614 Total Reflection Study of Bentonite Settled onto Magnetite, *The Journal of Physical Chemistry*
615 *C* 112(42) (2008) 16609-16615. <https://doi.org/10.1021/jp8048923>.

616 [21] W.N. Hansen, Electric Fields Produced by the Propagation of Plane Coherent
617 Electromagnetic Radiation in a Stratified Medium, *J. Opt. Soc. Am.* 58(3) (1968) 380-390.
618 <https://doi.org/10.1364/josa.58.000380>.

619 [22] W.N. Hansen, Expanded formulas for attenuated total reflection and the derivation of
620 absorption rules for single and multiple ATR spectrometer cells, *Spectrochimica Acta* 21(4)
621 (1965) 815-833. [https://doi.org/10.1016/0371-1951\(65\)80039-X](https://doi.org/10.1016/0371-1951(65)80039-X).

622 [23] R.T. Cygan, J.-J. Liang, A.G. Kalinichev, Molecular Models of Hydroxide, Oxyhydroxide,
623 and Clay Phases and the Development of a General Force Field, *J. Phys. Chem. B* 108(4) (2004)
624 1255-1266. <https://doi.org/10.1021/jp0363287>.

625 [24] E. Ferrage, B.A. Sakharov, L.J. Michot, A. Delville, A. Bauer, B. Lanson, S. Grangeon,
626 G. Frapper, M. Jiménez-Ruiz, G.J. Cuello, Hydration Properties and Interlayer Organization of
627 Water and Ions in Synthetic Na-Smectite with Tetrahedral Layer Charge. Part 2. Toward a
628 Precise Coupling between Molecular Simulations and Diffraction Data, *The Journal of Physical*
629 *Chemistry C* 115(5) (2011) 1867-1881. <https://doi.org/10.1021/jp105128r>.

630 [25] A. Delville, Modeling the clay-water interface, *Langmuir* 7(3) (1991) 547-555.
631 <https://doi.org/10.1021/la00051a022>.

632 [26] E. Rinnert, C. Carteret, B. Humbert, G. Fragneto-Cusani, J.D.F. Ramsay, A. Delville, J.-
633 L. Robert, I. Bihannic, M. Pelletier, L.J. Michot, Hydration of a Synthetic Clay with Tetrahedral
634 Charges: A Multidisciplinary Experimental and Numerical Study, *The Journal of Physical*
635 *Chemistry B* 109(49) (2005) 23745-23759. <https://doi.org/10.1021/jp050957u>.

636 [27] P. Porion, A.M. Faugère, A. Delville, ¹H and ⁷Li NMR Pulsed Gradient Spin Echo
637 Measurements and Multiscale Modeling of the Water and Ionic Mobility within Aqueous

638 Dispersions of Charged Anisotropic Nanoparticles, *The Journal of Physical Chemistry C*
639 112(31) (2008) 11893-11900. <https://doi.org/10.1021/jp802928n>.

640 [28] P. Porion, L.J. Michot, A.M. Faugère, A. Delville, Structural and Dynamical Properties of
641 the Water Molecules Confined in Dense Clay Sediments: a Study Combining ²H NMR
642 Spectroscopy and Multiscale Numerical Modeling, *The Journal of Physical Chemistry C*
643 111(14) (2007) 5441-5453. <https://doi.org/10.1021/jp067907p>.

644 [29] M. Jiménez-Ruiz, E. Ferrage, A. Delville, L.J. Michot, Anisotropy on the Collective
645 Dynamics of Water Confined in Swelling Clay Minerals, *The Journal of Physical Chemistry A*
646 116(10) (2012) 2379-2387. <https://doi.org/10.1021/jp201543t>.

647 [30] I. Bérend, J.-M. Cases, M. François, J.-P. Uriot, L. Michot, A. Masion, F. Thomas,
648 Mechanism of Adsorption and Desorption of Water Vapor by Homoionic Montmorillonites: 2.
649 The Li⁺ Na⁺, K⁺, Rb⁺ and Cs⁺-Exchanged Forms, *Clays and Clay Minerals* 43(3) (1995) 324-
650 336. <https://doi.org/10.1346/ccmn.1995.0430307>.

651 [31] S. Plimpton, Fast Parallel Algorithms for Short-Range Molecular Dynamics, *Journal of*
652 *Computational Physics* 117(1) (1995) 1-19. <https://doi.org/10.1006/jcph.1995.1039>.

653 [32] P.H. Axelsen, M.J. Citra, Orientational order determination by internal reflection infrared
654 spectroscopy, *Progress in Biophysics and Molecular Biology* 66(3) (1996) 227-253.
655 [https://doi.org/10.1016/S0079-6107\(97\)00007-2](https://doi.org/10.1016/S0079-6107(97)00007-2).

656 [33] K. Ohta, H. Ishida, Matrix formalism for calculation of electric field intensity of light in
657 stratified multilayered films, *Appl. Opt.* 29(13) (1990) 1952-1959.
658 <https://doi.org/10.1364/ao.29.001952>.

659 [34] K. Ohta, H. Ishida, Matrix formalism for calculation of the light beam intensity in stratified
660 multilayered films, and its use in the analysis of emission spectra, *Appl. Opt.* 29(16) (1990)
661 2466-2473. <https://doi.org/10.1364/ao.29.002466>.

662 [35] N.J. Harrick, Electric Field Strengths at Totally Reflecting Interfaces, *J. Opt. Soc. Am.*
663 55(7) (1965) 851-857. <https://doi.org/10.1364/josa.55.000851>.

664 [36] N.J. Harrick, F.K. du Pré, Effective Thickness of Bulk Materials and of Thin Films for
665 Internal Reflection Spectroscopy, *Appl. Opt.* 5(11) (1966) 1739-1743.
666 <https://doi.org/10.1364/ao.5.001739>.

667 [37] A. Bagchi, R.G. Barrera, A.K. Rajagopal, Perturbative approach to the calculation of the
668 electric field near a metal surface, *Physical Review B* 20(12) (1979) 4824-4838.
669 <https://doi.org/10.1103/PhysRevB.20.4824>.

670 [38] J.E. Sipe, Bulk-selvedge coupling theory for the optical properties of surfaces, *Physical*
671 *Review B* 22(4) (1980) 1589-1599. <https://doi.org/10.1103/PhysRevB.22.1589>.

672 [39] P.J. Feibelman, Surface electromagnetic fields, *Progress in Surface Science* 12(4) (1982)
673 287-407. [https://doi.org/10.1016/0079-6816\(82\)90001-6](https://doi.org/10.1016/0079-6816(82)90001-6).

674 [40] T. Higashiyama, T. Takenaka, Infrared attenuated total reflection spectra of adsorbed
675 layers at the interface between a germanium electrode and an aqueous solution of sodium
676 laurate, *The Journal of Physical Chemistry* 78(9) (1974) 941-947.
677 <https://doi.org/10.1021/j100602a016>.

678 [41] F. Takeda, M. Matsumoto, T. Takenaka, Y. Fujiyoshi, Studies of poly- γ -methyl-l-
679 glutamate monolayers by infrared ATR and transmission spectroscopy and electron
680 microscopy, *Journal of Colloid and Interface Science* 84(1) (1981) 220-227.
681 [https://doi.org/10.1016/0021-9797\(81\)90278-2](https://doi.org/10.1016/0021-9797(81)90278-2).

682 [42] W.-H. Jang, J.D. Miller, Molecular Orientation of Langmuir-Blodgett and Self-Assembled
683 Monolayers of Stearate Species at a Fluorite Surface As Described by Linear Dichroism
684 Theory, *The Journal of Physical Chemistry* 99(25) (1995) 10272-10279.
685 <https://doi.org/10.1021/j100025a031>.

686 [43] T. Buffeteau, M. Pézolet, Linear Dichroism in Infrared Spectroscopy, in: J.M. Chalmers,
687 P.R. Griffiths (Eds.), *Handbook of Vibrational Spectroscopy* 2001.
688 <https://doi.org/10.1002/0470027320.s0501>.

689 [44] F. Picard, T. Buffeteau, B. Desbat, M. Auger, M. Pézolet, Quantitative orientation
690 measurements in thin lipid films by attenuated total reflection infrared spectroscopy,
691 *Biophysical Journal* 76(1) (1999) 539-551. [https://doi.org/10.1016/s0006-3495\(99\)77222-x](https://doi.org/10.1016/s0006-3495(99)77222-x).

692 [45] M.J. Citra, P.H. Axelsen, Determination of molecular order in supported lipid membranes
693 by internal reflection Fourier transform infrared spectroscopy, *Biophysical Journal* 71(4) (1996)
694 1796-1805. [https://doi.org/10.1016/s0006-3495\(96\)79380-3](https://doi.org/10.1016/s0006-3495(96)79380-3).

695 [46] T. Easwarakhanthan, S. Ravelet, P. Renard, An ellipsometric procedure for the
696 characterization of very thin surface films on absorbing substrates, *Applied Surface Science*
697 90(2) (1995) 251-259. [https://doi.org/10.1016/0169-4332\(95\)00084-4](https://doi.org/10.1016/0169-4332(95)00084-4).

698 [47] W.J. Anderson, W.N. Hansen, Optical characterization of thin films*, *J. Opt. Soc. Am.*
699 67(8) (1977) 1051-1058. <https://doi.org/10.1364/josa.67.001051>.

700 [48] R.H.A. Ras, Y. Umemura, C.T. Johnston, A. Yamagishi, R.A. Schoonheydt, Ultrathin
701 hybrid films of clay minerals, *Physical Chemistry Chemical Physics* 9(8) (2007) 918-932.
702 <https://doi.org/10.1039/b610698f>.

703 [49] R.T. Cygan, J.-J. Liang, A.G. Kalinichev, Molecular Models of Hydroxide, Oxyhydroxide,
704 and Clay Phases and the Development of a General Force Field, *The Journal of Physical*
705 *Chemistry B* 108(4) (2004) 1255-1266. <https://doi.org/10.1021/jp0363287>.

706 [50] J.P. Larentzos, J.A. Greathouse, R. Cygan, An ab Initio and Classical Molecular Dynamics
707 Investigation of the Structural and Vibrational Properties of Talc and Pyrophyllite, *The Journal*
708 *of Physical Chemistry C* 111(34) (2007) 12752-12759. <https://doi.org/10.1021/jp072959f>.

709 [51] R.T. Cygan, J.A. Greathouse, H. Heinz, A.G. Kalinichev, Molecular models and
710 simulations of layered materials, *J. Mater. Chem.* 19(17) (2009) 2470.
711 <https://doi.org/10.1039/b819076c>.

712 [52] G.W. Brindley, G. Brown, M. Society, *Crystal Structures of Clay Minerals and Their X-*
713 *ray Identification*, Mineralogical Society 1980. <https://doi.org/10.1180/mono-5>.

714 [53] R. Fraser, T. MacRae, *Conformation in fibrous proteins and related synthetic polypeptides*,
715 Academic Press, New York, 1973. <https://doi.org/10.1016/B978-0-12-266850-0.X5001-X>.

716 [54] L. Pauling, E.B. Wilson, *Introduction to Quantum Mechanics with Applications to*
717 *Chemistry*, Dover Publications 2012. <https://doi.org/10.1038/136972a0>.

718 [55] C.T. Johnston, G.S. Premachandra, Polarized ATR-FTIR Study of Smectite in Aqueous
719 Suspension, *Langmuir* 17(12) (2001) 3712-3718. <https://doi.org/10.1021/la010184a>.

720 [56] J.L. Suter, P.V. Coveney, H.C. Greenwell, M.-A. Thyveetil, Large-Scale Molecular
721 Dynamics Study of Montmorillonite Clay: Emergence of Undulatory Fluctuations and
722 Determination of Material Properties, *The Journal of Physical Chemistry C* 111(23) (2007)
723 8248-8259. <https://doi.org/10.1021/jp070294b>.

724 [57] M.-A. Thyveetil, P.V. Coveney, J.L. Suter, H.C. Greenwell, Emergence of undulations and
725 determination of materials properties in large-scale molecular dynamics simulation of layered

726 double hydroxides Chem. Mater. 19(23) (2007) 5510-5523.
727 <https://doi.org/10.1021/cm070923u>.

728 [58] B. Carrier, M. Vandamme, R.J.M. Pellenq, M. Bornert, E. Ferrage, F. Hubert, H. Van
729 Damme, Effect of Water on Elastic and Creep Properties of Self-Standing Clay Films,
730 Langmuir 32(5) (2016) 1370-1379. <https://doi.org/10.1021/acs.langmuir.5b03431>.

731 [59] J.M. Cases, I. Berend, G. Besson, M. Francois, J.P. Uriot, F. Thomas, J.E. Poirier,
732 Mechanism of adsorption and desorption of water vapor by homoionic montmorillonite. 1. The
733 sodium-exchanged form, Langmuir 8(11) (1992) 2730-2739.
734 <https://doi.org/10.1021/la00047a025>.

735 [60] M. Szczerba, A. Kuligiewicz, A. Derkowski, V. Gionis, G.D. Chryssikos, A.G. Kalinichev,
736 Structure and Dynamics of Water-Smectite Interfaces: Hydrogen Bonding and the Origin of the
737 Sharp O-Dw/O-Hw Infrared Band From Molecular Simulations, Clays and Clay Minerals 64(4)
738 (2016) 452-471. <https://doi.org/10.1346/ccmn.2016.0640409>.

739 [61] R.H.A. Ras, J. Németh, C.T. Johnston, I. Dékány, R.A. Schoonheydt, Orientation and
740 conformation of octadecyl rhodamine B in hybrid Langmuir–Blodgett monolayers containing
741 clay minerals, Physical Chemistry Chemical Physics 6(23) (2004) 5347-5352.
742 <https://doi.org/10.1039/b411339j>.

743 [62] T. Dabat, F. Hubert, E. Paineau, P. Launois, C. Laforest, B. Grégoire, B. Dazas, E. Tertre,
744 A. Delville, E. Ferrage, A general orientation distribution function for clay-rich media, Nature
745 Communications 10(1) (2019) 5456. [10.1038/s41467-019-13401-0](https://doi.org/10.1038/s41467-019-13401-0).

746 [63] P. Podsiadlo, A.K. Kaushik, E.M. Arruda, A.M. Waas, B.S. Shim, J. Xu, H. Nandivada,
747 B.G. Pumplun, J. Lahann, A. Ramamoorthy, N.A. Kotov, Ultrastrong and Stiff Layered Polymer
748 Nanocomposites, Science 318(5847) (2007) 80-83. <https://doi.org/10.1126/science.1143176>.

749 [64] C. Aulin, G. Salazar-Alvarez, T. Lindström, High strength, flexible and transparent
750 nanofibrillated cellulose–nanoclay biohybrid films with tunable oxygen and water vapor
751 permeability, Nanoscale 4(20) (2012) 6622-6628. <https://doi.org/10.1039/c2nr31726e>.

752 [65] X.-F. Pan, H.-L. Gao, Y. Lu, C.-Y. Wu, Y.-D. Wu, X.-Y. Wang, Z.-Q. Pan, L. Dong, Y.-
753 H. Song, H.-P. Cong, S.-H. Yu, Transforming ground mica into high-performance biomimetic
754 polymeric mica film, Nature Communications 9(1) (2018) 2974.
755 <https://doi.org/10.1038/s41467-018-05355-6>.

756 [66] Q. Wang, J.L. Mynar, M. Yoshida, E. Lee, M. Lee, K. Okuro, K. Kinbara, T. Aida, High-
757 water-content mouldable hydrogels by mixing clay and a dendritic molecular binder, Nature
758 463(7279) (2010) 339-343. <https://doi.org/10.1038/nature08693>.

759

760

761

762